Total water levels along the South Atlantic Bight during three along-shelf propagating tropical cyclones: relative contributions of storm surge and wave runup

Chu-En Hsu[1], Katherine A. Serafin[2], Xiao Yu[1], Christie A. Hegermiller[3], John C. Warner[4], Maitane Olabarrieta[1]

[1]Department of Civil and Coastal Engineering, University of Florida, Gainesville, FL 32611, USA
5 [2]Department of Geography, University of Florida, Gainesville, FL 32611, USA
[3]Department of Civil and Environmental Engineering, University of Washington, Seattle, WA 98195, USA
[4]U.S. Geological Survey, Woods Hole, MA 02543, USA

Correspondence to: Chu-En Hsu (chuen.hsu@ufl.edu)

Abstract. Total water levels (*TWL*s), including the contribution of wind waves, associated with tropical cyclones (TC) are
10 among the most damaging hazards faced by coastal communities. TC–induced economic losses are expected to increase because of stronger TC intensity, sea level rise, and increased populations along the coasts. TC intensity, translation speed, and distance to the coast affect the magnitude and duration of increased *TWL*s and wind waves. Under climate change, the proportion of high–intensity TCs are projected to increase globally, whereas the variation pattern of TC translation speed also depends on ocean basin and latitude. There is an urgent need to improve our understanding of the linkages among TC
15 characteristics and *TWL* components. In the past years, hurricanes Matthew (2016), Dorian (2019), and Isaias (2020) propagated over the South Atlantic Bight (SAB) with similar paths but resulted in different coastal impacts. We combined *in situ* observations and numerical simulations with the Coupled Ocean–Atmosphere–Wave–Sediment Transport (COAWST) modeling system to analyze the extreme *TWL*s under the three TCs. Model verification showed that the *TWL* components were well reproduced by the present model setup. Our results showed that the peak storm surge and the peak wave runup depended
20 mainly on the TC intensity, the distance to the TC eye, and the TC heading direction. A decrease of TC translation speed primarily led to longer exceedance durations of *TWL*s, which may result in more severe economic losses. Wave–dependent water level components (i.e., wave setup and wave swash) were found to dominate the peak *TWL* within the near–TC field. Our results also showed that in specific conditions, the pre–storm wave runup associated with the TC–induced swell may lead to *TWL*s higher than at the peak of the storm. This was the case along the SAB during Hurricane Isaias. Isaias's fast TC
25 translation speed and the fact that its swell was not blocked by any islands were the main factors contributing to these peak *TWL*s ahead of the storm peak.

1 Introduction

Total water levels (*TWL*s), defined as the combination of astronomic tides, mean sea level, storm surge, and wave runup (combination of wave setup and wave swash), associated with tropical cyclones (TC) are among the leading hazards faced by
30 coastal communities (e.g., Kalourazi et al., 2020; Sallenger, 2000). The Saffir–Simpson Hurricane Wind Scale (SSHWS) has

been used to estimate the potential impacts and economic losses caused by TCs based on the maximum sustained wind speed. However, the maximum sustained wind speed, the TC translation speed (Liu et al., 2007; Xu et al., 2007), the size of the storm (Irish et al., 2008), and the storm track (Suh and Lee, 2018; Wang et al., 2020) affect wave heights, wave periods, and storm surge levels along the coast differently. Alipour et al. (2022) pointed out that using SSHWS as a proxy of the expected impacts

35 alone may lead to severe miscalculation, and they proposed a new scaling system associated with rainfall, storm surge, and wind speed. Irish and Resio (2010) proposed a hydrodynamics–based surge scale for hurricane surge hazard and an approach for predicting expected flood inundation and economic losses. Sallenger (2000) proposed a more complex approach in which the TWL relative to the dune crest (D_{crest}) and dune base (D_{base}) elevations was used to classify four expected morphological impact regimes: swash ($TWL < D_{base}$), collision ($D_{base} \leq TWL < D_{crest}$), overwash and inundation ($D_{crest} \leq TWL$). In the

40 overwash regime TWL exceeds D_{crest} when the wave swash effects are accounted for. In the inundation regime TWL exceeds D_{crest} even without the effect of the wave swash. Among these regimes, coastal dunes experience the direct impacts of surf–zone processes in the inundation regime, when TWL exceeds D_{crest}. Thus, the inundation regime is expected to induce the highest economic losses among the four impact regimes while the swash regime represents the least severe condition with less anticipated economic losses. TWL thus represents the combination of storm independent (the mean sea level and astronomic

45 tides) and storm dependent (wave runup and storm surge) water level components, being a better indicator of the increased water levels than the storm surge alone (Stockdon et al., 2007). We assume that astronomic tides and storms are at first order independent, although extreme winds and storm surges can interact with the tidal wave and cause tidal distortions (e.g., Paniagua-Arroyave et al., 2019). The wave runup is a wind wave dependent parameter composed by a wave–averaged sea level variation known as 'wave setup' and a wave–varying fluctuating component known as 'wave swash' (Stockdon et al.,

50 2006). Previous efforts have shown the complexity and uncertainty of TC–induced surges and compound floods. However, the response of TWL to storm characteristics is more complicated than that corresponding to the storm surge, and the relative role of the wave runup and storm surge, and the dependency with storm characteristics are still poorly understood.

There are primarily two approaches for computing TWLs during extreme storms: with numerical models (e.g., Hegermiller et al., 2019) and with observed water levels and waves (e.g., Serafin and Ruggiero, 2014). For example, η_0 (i.e., the sum of

55 astronomic tides, mean sea level, and storm surge) observations were available at National Oceanic and Atmospheric Administration (NOAA; https://tidesandcurrents.noaa.gov/) tide gauges. Coupled ocean–wave modeling systems such as Coupled Ocean–Atmosphere–Wave–Sediment Transport model (COAWST; Warner et al., 2010) can also be applied to predict η_0 deterministically and probabilistically. However, the wave runup component needed to compute the TWL is not captured by tide gauges, and regional ocean models usually do not have sufficient spatial resolution to reproduce the wave setup

60 accurately. Moreover, due to the use of phase–averaged models, coupled modeling systems such as ROMS–SWAN are not able to reproduce the wave swash component. While models such as InWave (Infragravity Wave model installed within COAWST; Olabarrieta et al., 2023) can solve infragravity waves, phase resolving models like FUNWAVE (Shi et al., 2012) can be applied to simulate the wave swash. However, InWave and FUNWAVE require higher resolution in space and time, which makes them relatively not efficient for large spatial areas.

65 To overcome this modeling challenge, the wave runup can be computed using empirical formulas and linearly added to η_0. For example, Serafin and Ruggiero (2014) applied the empirical formula proposed by Stockdon et al. (2006) to compute the wave runup at NOAA tide gauges using the wave parameters observed at nearby National Data Buoy Center (NDBC; https://www.ndbc.noaa.gov/) wave buoys along the U.S. West Coast. While the wave runup of Stockdon et al. (2006) formulation is represented by a linear increase with increasing deep–water zero–order moment wave height (H_0), Senechal et

70 al. (2011) suggested an upper limit of wave runup at highly dissipative beaches under energetic conditions (e.g., tropical cyclone). Senechal et al. (2011) proposed another empirical formula for wave runup based on wave height alone, to avoid the over–prediction under such scenarios, and stated that the saturation of wave runup required further studies and measurements under diverse beach scenarios before generalization. Despite the importance of the wave runup in *TWL* estimation, the sensitivity of wave runup to the choice of these formulas had not been thoroughly examined. In the meantime, the sensitivity

75 and the applicability of these formulas under different storm conditions are poorly understood.

Parker et al. (2023) recently characterized the relative contributions of astronomic tides, storm surge and wave setup to extreme water levels along the U.S. Southeast Coast, discovering regional patterns in the average contributions of waves and storm surge to extreme water levels over the 38–year hindcast. Here, we analyzed how TC characteristics affect the relative contributions of storm surge and wave runup to *TWL*s and their impacts by applying the COAWST modeling system to simulate

80 *TWL*s along the South Atlantic Bight (SAB; extending from North Carolina to Florida) during three historical TCs with similar tracks. In the recent past, three hurricanes (Matthew 2016, Dorian 2019, and Isaias 2020) propagated through the shelf of the SAB with similar tracks (Fig 1). The average TC characteristics and the associated economic losses of these three TCs according to the International Best Track Archive for Climate Stewardship (IBTrACS; Knapp et al., 2018; https://www.ncei.noaa.gov/products/international-best-track-archive) are indicated in Table 1. While the economic loss from

85 Matthew ($10.0 billion; Stewart, 2017) was the highest from all storms, it was one order of magnitude higher than that of Dorian ($1.6 billion by Dorian; Avila et al., 2020), even with similar maximum sustained wind speeds (V_{max}). Surprisingly, while Dorian had a stronger intensity than Isaias according to the SSHWS, Isaias caused higher economic loss. ($4.8 billion; Latto et al., 2021) Isaias had the fastest translation speed (V_t) across all three hurricanes within the SAB, whereas Dorian had the slowest V_t and the smallest radius of maximum wind (R_{max}) on average. How the differences in V_{max}, V_t, and distance to

90 the coast influenced the *TWL* components during these three TCs is still not well understood. With similar tracks over the SAB, these three historical TCs provided the opportunity to determine the effects of each TC property on waves and *TWL* along the coast. Because the proportion of high–intensity TCs (i.e., SSHWS category 4 to 5) and the corresponding maximum sustained wind are projected to increase at the global scale (Masson-Delmotte et al., 2021) due to climate change, understanding how TC characteristics influence the makeup of the *TWL* is essential for preparing for future coastal impacts.

95

Table 1. Averaged values of TC parameters of the three historical hurricanes within the SAB. The values were calculated from the International Best Track Archive for Climate Stewardship (IBTrACS) and National Hurricane Center datasets. V_t is the translation speed of storms; V_{max} is the maximum sustained wind; P_{min} is the minimum atmosphere pressure; R_{max} is the radius of maximum wind; economic loss is estimated in billion USD.

Hurricane	V_t (m s^{-1})	V_{max} (m s^{-1})	P_{min} (mb)	R_{max} (km)	Economic loss (billion USD)
Matthew	6.17	45.25	959.44	52.67	10.0
Dorian	3.27	58.80	945.36	35.52	1.6
Isaias	6.26	32.11	993.06	53.38	4.8

100
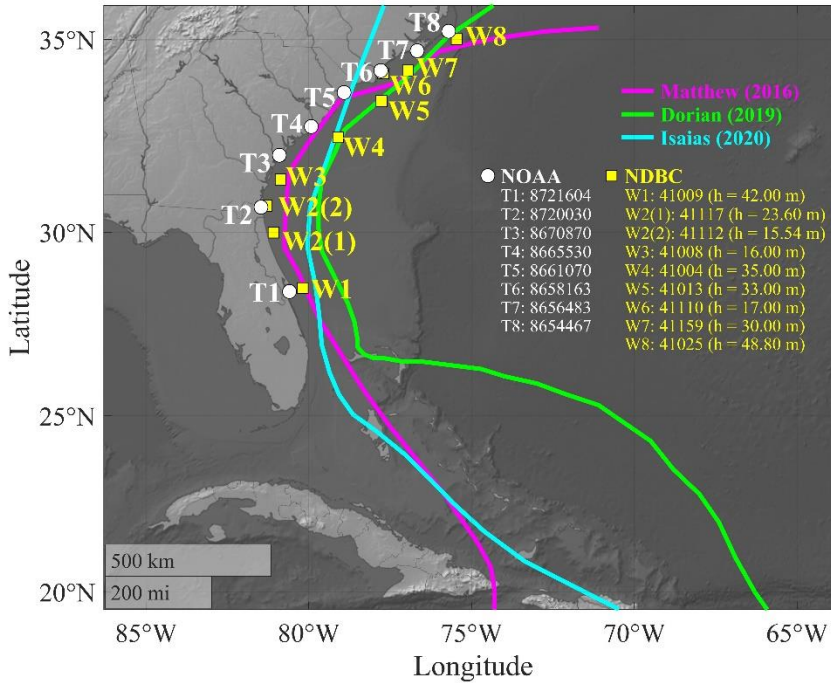
Figure 1. Best tracks of hurricanes Matthew 2016 (magenta), Dorian 2019 (green), and Isaias 2020 (cyan) and NOAA tide gauges (white circles), NDBC wave buoys (yellow squares) selected for the model verification. *h* represents the water depth.

This paper is organized as follows: a brief review of the modeling system and model setup is presented following the

105 introduction. Model verification based on the comparison with historical observations at eight NOAA tide gauges can be found next. *TWL* components along the SAB during Matthew 2016, Dorian 2019, and Isaias 2020 are analyzed and compared in the result and discussion section. The applicability of the two empirical wave runup formulas and the effect of TC characteristics on wave runup are also discussed and presented.

2 Methods

110 Following the modeling framework of Hegermiller et al. (2019), we configured COAWST as a coupled ocean–wave model and set it up to simulate the ocean and wave dynamics during hurricanes Matthew (2016), Dorian (2019) and Isaias (2020). Ocean dynamics were resolved with the Regional Ocean Modeling System (ROMS; Shchepetkin and McWilliams, 2005),

while wind wave generation and propagation were simulated with Simulating WAves Nearshore (SWAN; Booij et al., 1999). The computational flowchart of the ocean circulation–wave coupling applied here is shown in the appendix (Fig. A1). The ocean and wave models used the same horizontal grids, with a 5 km resolution parent grid covering the entire U.S. East Coast and a 1 km resolution child grid covering the southern SAB.

2.1 Ocean model (ROMS)

ROMS solves the Reynolds Averaged Navier–Stokes equations (RANS) utilizing a three–dimensional terrain–following framework with a curvilinear coordinate transformation and finite–difference approximations (Shchepetkin and McWilliams, 2005). Additional information on the wave–current closures models included in ROMS is provided in Kumar et al. (2012), Warner et al. (2008), and Warner et al. (2010).

2.2 Wave model (SWAN)

The third–generation spectral wave model SWAN (Booij et al., 1999) solves the wave action evolution while considering refraction, shoaling, wave–current interactions, wind–wave generation, and varied wave energy dissipation (bottom friction, breaking, and white–capping). The semi–empirical formula derived from the JOint North Sea WAve Project (JONSWAP) was used to calculate bottom friction (Hasselmann et al., 1973). We calculated wind wave growth and white–capping using the formulas presented by Komen et al. (1984). We used discrete interaction approximation (DIA; Hasselmann et al., 1985) for the non–linear quadruplet wave–wave interactions.

2.3 Model setup

In the current work, winds, atmospheric pressure, relative humidity, and surface air temperature from the RAPid refresh (RAP) re–analyzed data (Benjamin et al., 2016; https://www.nco.ncep.noaa.gov/pmb/products/rap/) were employed to force ROMS. This dataset comprised atmospheric pressure at mean sea level (MSL) and wind speeds 10 meters above MSL. Although RAP only covers a portion of the computational domain, it has a spatial resolution of 13 km at hourly time intervals. The Global Forecast System (GFS; 50 km resolution with a 3–hour time interval; https://www.ncdc.noaa.gov/data-access/model-data/model-datasets/global-forcast-system-gfs) provided wind and atmospheric pressure forces for offshore regions that RAP did not cover.

The U.S. East Coast domain had a horizontal grid resolution of 5 km with 896 (ξ–direction) ×336 (η–direction) grid cells. The SAB domain had a horizontal grid resolution of 1 km with 272 (ξ–direction) ×376 (η–direction) grid cells. The numerical grids of ROMS had 16 vertical layers. For the SAB grid and the U.S. East Coast grid, the baroclinic time steps in ROMS were 30 seconds and 15 seconds, respectively. To determine the initial conditions for the surface water levels, velocities, salinity, and temperature, we used the re–analyzed data from the HYbrid Coordinate Ocean Model (HYCOM; Metzger et al., 2014; https://www.ncei.noaa.gov/thredds-coastal/catalog/hycom_region1/catalog.html). 13 tidal elements (M2, S2, N2, K1, K2, O1, P1, Q1, MF, MM, M4, MS4, and MN4) from the TPXO Tide Model database at Oregon State University (Egbert and Erofeeva,

2002) were applied to the parent grid to simulate astronomic tides. The Flather boundary condition (Flather, 1976) was applied at the boundaries of the ROMS model (the northeast and southeast boundaries of the black–dashed box in panel a of Fig. A2 in the appendix) for the momentum balance to radiate out deviations from exterior values at the speed of the external ocean waves. A two–day spin–up was done, followed by an 11–day simulation (i.e., 13 days in total). The initial conditions, such as currents, water levels, temperature, and salinity, were examined to show that the two–day spin–up is adequate for them to achieve the equilibrium state in the model. It was determined that an 11–day simulation period, including at least five days prior to the storm's peak, was sufficient to track the development and spread of swells near the SAB.

For the boundary conditions of the SWAN model for Hurricane Matthew, hourly statistical wave bulk parameters (zero–order moment wave height, mean wave direction, and peak wave period) from NOAA's WAVEWATCH III re–analyzed global dataset (The WAVEWATCH III Development Group, 2016; https://polar.ncep.noaa.gov/waves/ensemble/download.shtml) were imposed at 47 boundary segments along the southeast and northeast boundaries of the U.S. East Coast grid (the black–dashed box in Fig. A2 in the appendix) assuming the JONSWAP wave spectra. NOAA's WAVEWATCH III re–analyzed global dataset did not have available data during Dorian and Isaias. Thus, we employed a larger grid to cover the North Atlantic Ocean and the Gulf of Mexico with our modeling system to generate the wave boundary conditions for these two TCs for input as boundary conditions to the SWAN model. Wave spectrum was solved with 60 and 25 directional and frequency bins. The parent and child grids were solved with 30 and 15 seconds as their computational time steps, respectively. As for the atmospheric forcing, SWAN used the same GFS–RAP input as ROMS.

Using the Model Coupling Toolkit, water levels, current velocities, and wave fields are two–way coupled in COAWST (Warner et al., 2008). In our simulations, the data exchange interval between ROMS and SWAN was set to 30 minutes, including water surface elevation, current velocities, statistical wave bulk parameters (e.g., zero–order moment wave heights, peak and mean wavelengths, peak and mean wave periods, peak and mean wave directions, and wave dissipation). This exchange interval has been tested and used by Hegermiller et al. (2019) and Hsu et al. (2023), in which the nearshore hydrodynamics was replicated adequately. Thereby, we applied the same data exchange interval in the present work. Specifics regarding the coupling method and an example case study were provided (Warner et al., 2008; 2010). The wind shear stresses and sea surface roughness by Taylor and Yelland (2001) at the sea surface were computed and used to force the ocean model. The vortex–force formulation (Kumar et al., 2012; Uchiyama et al., 2010) was employed in the current study to account for wave–current interaction. Furthermore, the wave and current boundary layer properties were estimated with the SSW_BBL option, which used the model of Madsen (1994).

2.4 Empirical formulas for wave runup

We followed the work of Serafin and Ruggiero (2014) and applied the empirical formulas proposed by Stockdon et al. (2006) and Senechal et al. (2011) to compute the wave runup at NOAA tide gauges using the wave parameters at nearby NDBC wave

buoys along the SAB. The locations of the tide gauges and wave buoys are indicated in Fig 1. The empirical formula proposed by Stockdon et al. (2006) (Eqs. 1 and 2) provides the 2% exceedance percentile of extreme wave runup (R_2):

$$R_2 = 1.1\left(0.35\beta_f(H_0L_0)^{\frac{1}{2}} + \frac{\left[H_0L_0\left(0.563\beta_f^2+0.004\right)\right]^{\frac{1}{2}}}{2}\right), \ 0.3 \leq \xi_0 < 4.0 , \tag{1}$$

$$R_2 = 0.043(H_0L_0)^{\frac{1}{2}}, \ \xi_0 < 0.3 , \tag{2}$$

180   in which foreshore beach slope (β_f) and deep–water wave parameters (H_0 is the deep–water zero–order moment wave height and L_0 is the deep–water peak wavelength) and the Iribarren number (ξ_0) (Eq. 3) were required. ξ_0 was used to categorize wave breaker types (Battjes, 1974). In Eq. 1, the first part ($1.1 \cdot 0.35\beta_f(H_0L_0)^{\frac{1}{2}}$) represents wave setup, and the second part ($1.1 \cdot \frac{\left[H_0L_0\left(0.563\beta_f^2+0.004\right)\right]^{\frac{1}{2}}}{2}$) represents the combination of infragravity swash and incident swash.

$$\xi_0 = \frac{\beta_f}{(H_0/L_0)^{1/2}} , \tag{3}$$

185   While beach slopes depend on local coastal morphology, wave heights and wavelengths also depend on storm characteristics. Stockdon et al. (2007) pointed out that the swash zone can be moved onshore along the beach profile due to the large waves and storm surges during extreme weathers. Consequently, the mean beach slope (β_m), measuring the slope of the beach from the shoreline to the dune base, was suggested and defined as the relevant slope in Eqs. 1 and 3 during hurricanes. The deep–water wave parameters can be calculated by de–shoaling the waves from a given point along the coast or shelf to deep water

190   using the linear wave theory. The empirical formula developed by Stockdon et al. (2006) separated intermediate to wave–reflective beach scenarios ($0.3<\xi_0<4.0$, Eq. 1) from extremely dissipative conditions ($\xi_0<0.3$, Eq. 2). According to their dataset, R_2 under $\xi_0<0.3$ did not necessarily linearly depend on the beach slope and was generally dominated by infragravity waves. Thus, Stockdon et al. (2006) suggested to use a parameterization with a similar form for infragravity swash to model the R_2 under $\xi_0<0.3$ (Eq. 2). While the field data employed by Stockdon et al. (2006) did not specifically include highly energetic

195   conditions during storms, Stockdon et al. (2014) compared the numerical simulated wave runup of XBeach (Roelvink et al., 2009) with the parameterized wave runup of Stockdon et al. (2006) under storm conditions. Stockdon et al. (2014) showed that the parameterized wave runups were consistent with XBeach model results for SSHWS category 1 scenario, while the wave runups associated with more energetic conditions still require further discussions.

    While R_2 in the Stockdon et al. (2006) formulation is represented by a linear increase with increasing H_0, Senechal et al. (2011)

200   suggested an upper limit of R_2 at highly dissipative beaches under energetic conditions (e.g., tropical cyclone). Senechal et al. (2011) proposed another empirical formula for R_2 based on H_0 alone (Eq. 4), to avoid the over–prediction under such scenarios.

$$R_2 = 2.14\tanh(0.4H_0) , \tag{4}$$

While the observed data used in Stockdon et al. (2006) included part of the study area of the present work (i.e., North Carolina), most of the scenarios (>93%) at the peaks of hurricanes Matthew, Dorian, and Isaias along the SAB belonged to intermediate beach conditions, on which Stockdon et al. (2006) primarily focused ($0.3<\xi_0<4.0$). On the contrary, Senechal et al. (2011) specifically considered dissipative beach conditions.

3 Model verification

We used the observed data from eight NOAA tide gauges and nine NDBC buoys along the SAB to verify the model performance (Fig. 1). These NOAA tide gauges and NDBC buoys were selected based on the observed data availability during the three hurricanes. Tide gauges T1, T7, and T8 are installed behind a barrier island, while tide gauge T2 is installed within an estuary. The other four tide gauges are installed at piers in local beaches. Thus, the measured *TWL*s at T1, T2, T7, and T8 may not reflect the exact water levels at the beach. The model performance on statistical wave bulk parameters (zero–order moment wave height, mean wave direction, and peak wave period) and the wave energy spectra resulting from the current model setup have been verified and discussed by Hsu et al. (2023). In the present study, we followed the approach of Serafin and Ruggiero (2014) to compute *TWL*s, including wave runup (R_2), and used the measurements at NOAA tide gauges (T1–T8) and the nearby NDBC wave buoys (W1–W8) as the 'observational data'. While seven of these NOAA tide gauges had corresponding NDBC buoys used for wave runup estimation, two NDBC buoys (W2(1) and W2(2)) were assigned to the tide gauge T2 (NOAA 8720030) for different storm events due to the lack of data. Wave parameters (zero–order moment wave height, H_{m0}, and peak wave period, T_P) at W1–W8 were used to estimate the corresponding R_2 at T1–T8 using the formula of Stockdon et al. (2006). We used the linear wave dispersion relation to compute the representative deep–water peak wave parameters (H_0 and L_0). For model results, we used the predicted H_{m0} and T_P extracted at the COAWST computational grid with the shortest distance to the U.S. Geological Survey (USGS; https://coastal.er.usgs.gov/data-release/doi-F7GF0S0Z/) data points along the SAB. The mean beach slopes measured by USGS before Hurricane Matthew along the SAB (Doran et al., 2015; Doran et al., 2017) were used to compute R_2 (Eq. 1). While USGS had some post–Matthew field surveys, these later measurements only covered a relatively small range or did not overlap with the SAB. To simplify the problem and to focus on the comparison of TC–induced water level components under the three historical TCs, the coastal morphology was assumed not to change between storms.

To quantify the model performance, we used the correlation coefficient between the "measured" and simulated peak storm surge, peak wave runup, and maximum continuous duration of $TWL \geq D_{base}$ at these eight NOAA tide gauges (Fig. 2). Overall, model results showed good agreement with NOAA observations: from the 24 data points at eight NOAA tide gauges during three storms with the correlation coefficient higher than 0.7 for the peak *TWL*, the peak storm surge (η_S), the peak wave runup (R_2), and the maximum continuous duration of $TWL \geq D_{base}$ (T_{TWL}). We utilized the Lanczos low–pass filter (Duchon, 1979) to remove the astronomic tides from η_0 and obtained the storm surge (η_S). It is noted that there were larger discrepancies of the peak η_S and T_{TWL}. There may be several reasons causing the discrepancy between observed and model results. For

example, the observed data at NOAA tide gauges may not reflect the actual extreme water levels and the corresponding durations at beach because of their locations, especially at tide gauges T1, T2, T7, and T8 which are located within estuaries or behind barrier islands. The current spatial resolution of the computational grid may not completely reflect the details of the bathymetry around these estuaries and narrow barrier islands. Secondly, the potential influence of rainfall and river discharge nearby these observed locations may also contribute to the *TWL*. As we used a low–pass filter to remove the contribution from astronomic tides, rainfall and river discharge may contribute to the resulting water level as well. Accordingly, we used the model results from the ROMS–SWAN model to focus on the storm–forced water level components induced by wind and atmospheric pressure at beaches along the SAB in the present work, which also allows for a higher spatial and temporal resolution of *TWL* at beach.
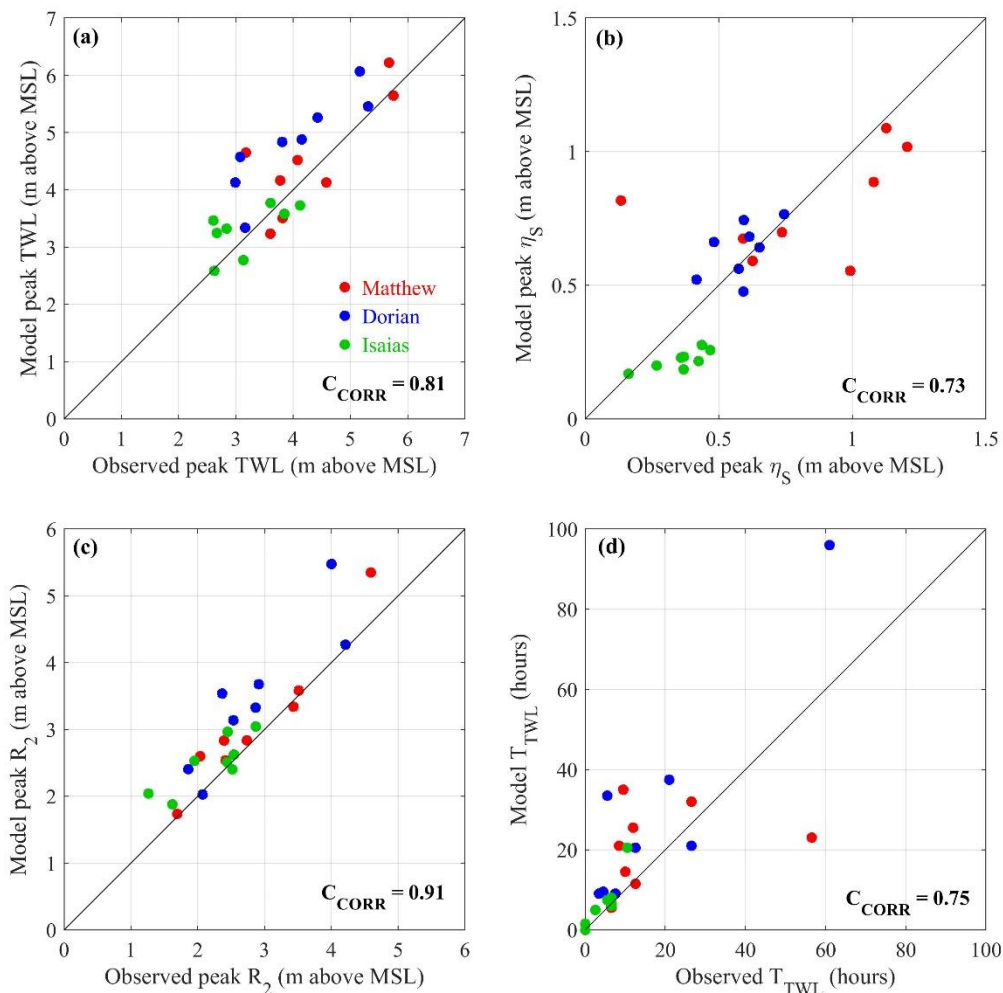
Figure 2. Model verification of (a) the peak *TWLs*, (b) the peak storm surge, (c) the peak wave runup, and (d) the maximum continuous duration of *TWL* $\geq D_{base}$ (T_{TWL}) at eight NOAA tide gauges during the three historical hurricanes. The red, blue, and green points denote the data of hurricanes Matthew, Dorian, and Isaias, respectively. The corresponding correlation coefficients (C_{CORR}) are shown on the bottom–right corner in each panel.

 4 Results and discussion

This section compares the temporal and spatial changes of η_S and R_2 along the SAB caused by hurricanes Matthew in 2016, Dorian in 2019, and Isaias in 2020. Additionally, the relationship between TC characteristics and the TC–induced water level components is examined.

4.1 Storm forced water level components

255   *TWL* depends on the astronomic tides, which is at first order independent of TC characteristics, in such a way that the peak of the TC–induced water level can occur at any tidal level. Here, we focused on the influences of V_{max}, V_t and TC path on two TC–induced water level components: η_S and R_2. We combined η_S with the R_2 estimated by the Stockdon et al. (2006) formulation to obtain the peak TC–induced water level, η_T (panels a1, b1, and c1 in Fig. 3).
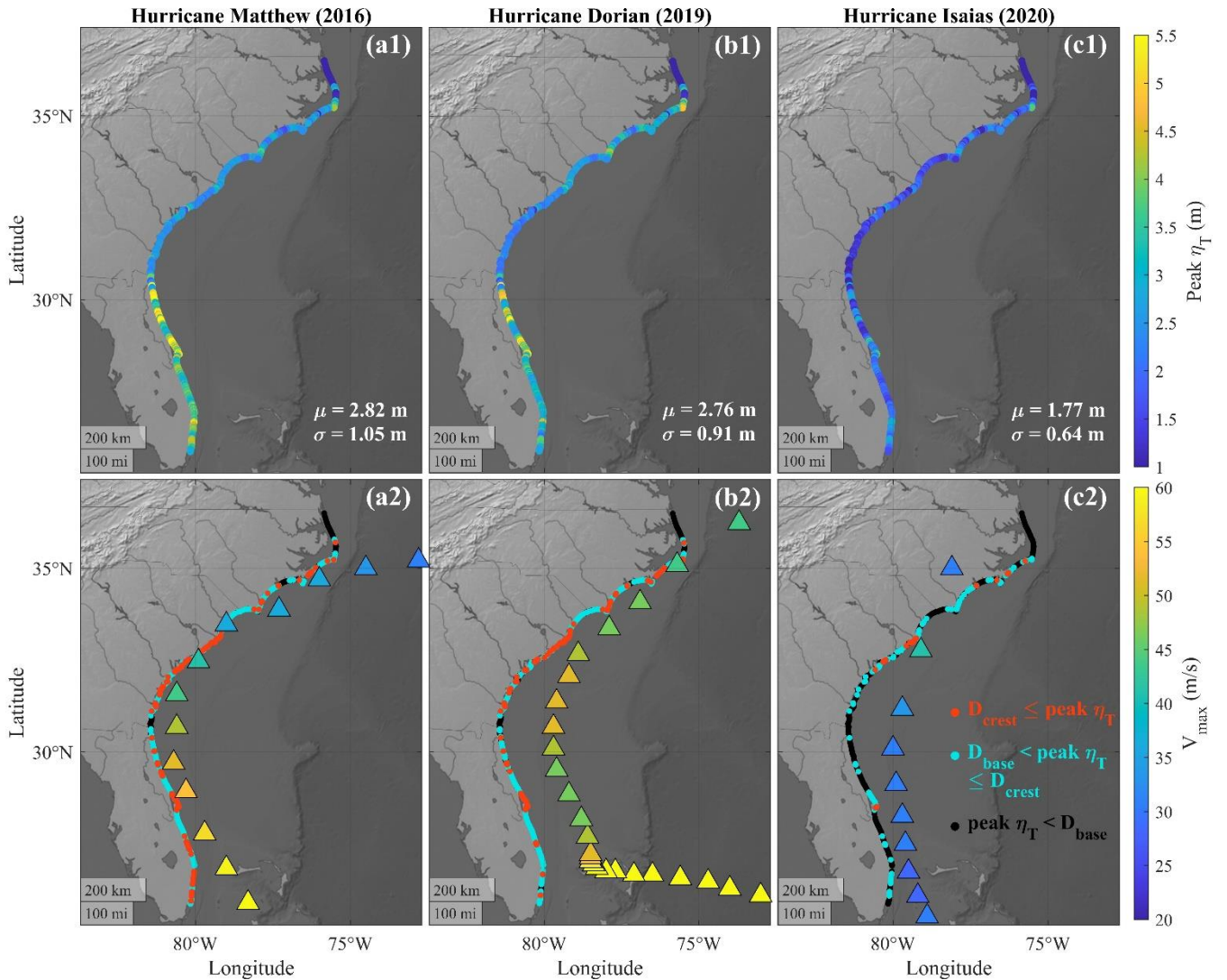
Figure 3. a1, b1, and c1) Peak η_T (i.e., the sum of η_S and R_2) along the SAB during the three hurricanes; μ represented the average and σ was the standard deviation along the SAB. a2, b2, and c2) IBTrACS data of the TC every six hours with the colormap presenting instantaneous maximum sustained wind (V_{max}); the red, blue, and black points indicated the most severe levels achieved during the TC. We followed Sallenger (2000) and used local D_{crest} and D_{base} elevations to categorize the peak η_T. These categorizations were $D_{crest} \leq$ peak η_T; $D_{base} \leq$ peak $\eta_T < D_{crest}$; and peak $\eta_T < D_{base}$.

4.2 Peak values and durations of η_T and *TWL* over specified thresholds along the SAB

Matthew and Dorian had stronger V_{max} on average (45.25 m s^{-1} and 58.80 m s^{-1} respectively) within the SAB compared to Isaias (32.11 m s^{-1}; Table 1), which led to lower surge levels during Isaias (15 cm to 90 cm lower than Matthew and Dorian). Meanwhile, Matthew's distance to the coastline (47.38 km) was shorter compared to Dorian (96.73 km) and Isaias (97.24 km) along the SAB on average. The peak η_T along the SAB showed similar values and distribution patterns during Matthew and Dorian, but was 60% to 65% smaller on average during Isaias (panels a1, b1, and c1 in Fig. 3). Along Florida's southeast coast

the peak η_T was higher during Matthew compared to Dorian and Isaias, but decreased significantly along Georgia and South Carolina as Matthew propagated northward and weakened. This led to a higher deviation of peak η_T along the SAB during Matthew compared to Dorian and Isaias.

We used D_{crest} and D_{base} as thresholds to categorize the peak η_T and *TWL* into the impact regimes of Sallenger (2000) along the SAB. The peak η_T can occur coincidently with either the high tide or the low tide. Without the astronomic tides, the present work isolated and determined the contribution of TC–induced water level components and its dependency on TC characteristics. While Sallenger (2000) used the thresholds to categorize the morphological impacts caused by the *TWL*s, we utilized the thresholds to categorize the levels of TC–induced water levels (η_T) specifically. 23.0% and 19.9% of the coastal sites experienced peak $\eta_T \geq D_{crest}$ (red points in panels a2, b2, and c2 of Fig. 3) during Matthew and Dorian, respectively. These percentages were higher during Matthew and Dorian compared to those during Isaias (3.5%) (Table 2).

Table 2. Percentage of coastal sites of each categorization of peak η_T and peak *TWL* during the three historical TCs along the SAB.

	Categorizations of the peak η_T			Categorizations of the peak *TWL*		
	$D_{crest} \leq$ peak η_T	$D_{base} \leq$ peak $\eta_T < D_{crest}$	peak $\eta_T < D_{base}$	$D_{crest} \leq$ peak *TWL*	$D_{base} \leq$ peak *TWL* $< D_{crest}$	peak *TWL* $< D_{base}$
Matthew	23.0%	55.6%	21.4%	41.6%	46.4%	12.0%
Dorian	19.9%	54.8%	25.3%	42.0%	49.2%	8.8%
Isaias	3.5%	22.1%	74.4%	18.7%	46.0%	35.3%

The proportion of coastal sites experiencing peak *TWL* $\geq D_{crest}$ was at least 1.8 times more than peak $\eta_T \geq D_{crest}$ (Table 2), which showed the importance of astronomic tides in coastal inundation levels. Matthew had a shorter distance to the coast along the SAB compared to Dorian, while Dorian had stronger intensity north to Georgia (Fig. 3 and Table 1). Consequently, Matthew and Dorian induced comparable peak η_T along the SAB.

In addition to the peak η_T, we used D_{base} as the threshold to compute the maximum continuous durations of $\eta_T \geq D_{base}$ (T_{ETA}; panels a1, b1, and c1 in Fig. 4) and *TWL* $\geq D_{base}$ (T_{TWL}; panels a2, b2, and c2 in Fig. 4) along the SAB throughout each of the entire storm events. These were determined by calculating the maximum continuous duration that η_T or *TWL* was higher than the thresholds without interruption. The D_{base} was applied here because less than 23% of all coastal sites experienced peak $\eta_T \geq D_{crest}$ during the three TCs (Table 2). The averaged T_{ETA} along the SAB during Dorian (55.1 hours) was longer than those during Matthew (32.5 hours) and Isaias (7.1 hours) (Fig. 4). Considering the contributions from astronomic tides, the averaged T_{TWL} along the SAB were 27.5, 32.9, and 6.7 hours during Matthew, Dorian, and Isaias, respectively (Fig. 4). Note that the difference of averaged T_{TWL} during Matthew and Dorian (i.e., 32.9−27.5=5.4 hours) was 76% smaller than the corresponding difference of averaged T_{ETA} (i.e., 55.1−32.5=22.6 hours). This was mainly related to the smaller tidal range during Hurricane Matthew compared to Dorian. Although *TWL* was larger than η_T at high tides (crests of astronomic tidal

signal), it was smaller than η_T at low tides (troughs of astronomic tidal signal). This pointed out the importance of the instantaneous tidal range in the inundation duration under extreme weather conditions.
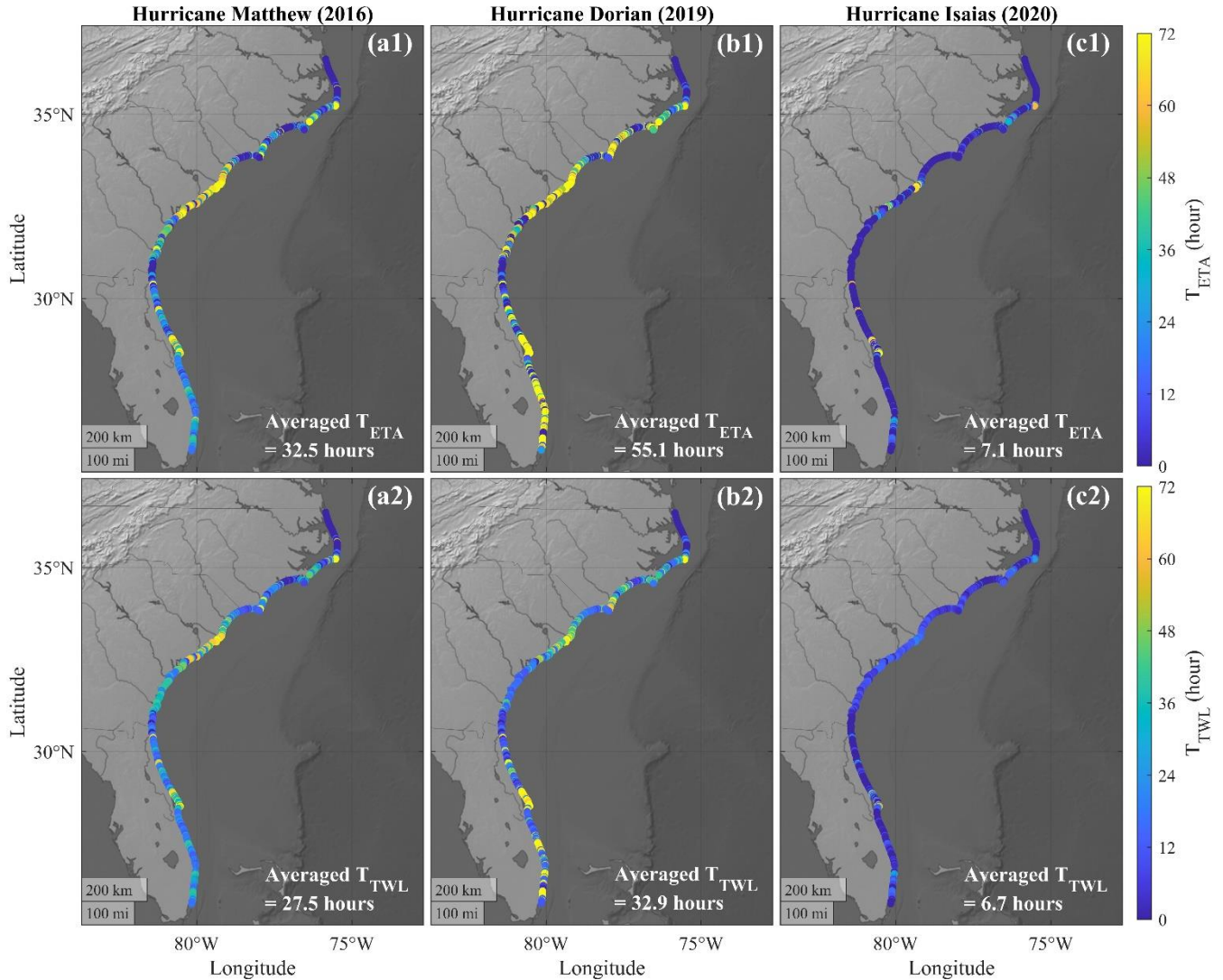
Figure 4. The maximum continuous duration of η_T (T_{ETA}; panels a1, b1, and c1) and *TWL* (T_{TWL}; panels a2, b2, and c2) over D_{base} at each USGS coastal site along the SAB throughout each of the three historical hurricanes.

We calculated the maximum continuous duration of d/R_{max} (i.e., normalized distance) ≤8.0 at each coastal site throughout each of the three storm events, where d was the distance between TC eye and each coastal site along the SAB and R_{max} was the instantaneous radius of maximum wind (Fig. 5). This threshold followed the distance threshold of near–TC field (Collins et al., 2018; Young, 2006). While Young (2006) also considered V_{max} in the definition of near–TC field, we did not consider the threshold for V_{max} here, because V_{max} was relatively small along the SAB during Isaias. We found the duration of d/R_{max} ≤8.0 had a correlation coefficient (C_{CORR}) = 0.47 with T_{ETA} considering the coastal sites along the SAB during

hurricanes Matthew, Dorian, and Isaias. In particular, the durations of $d/R_{max} \leq 8.0$ during Matthew and Dorian (Fig. 5)

310   showed similar patterns as T_{ETA} (panels a1, b1, and c1 in Fig. 4). Meanwhile, the path of Hurricane Isaias had short distances to Florida's southeast coast and resulted in the duration of $d/R_{max} \leq 8.0$ longer than 48 hours. However, it did not lead to longer T_{ETA}, primarily because of the weaker V_{max} of Isaias along the SAB.
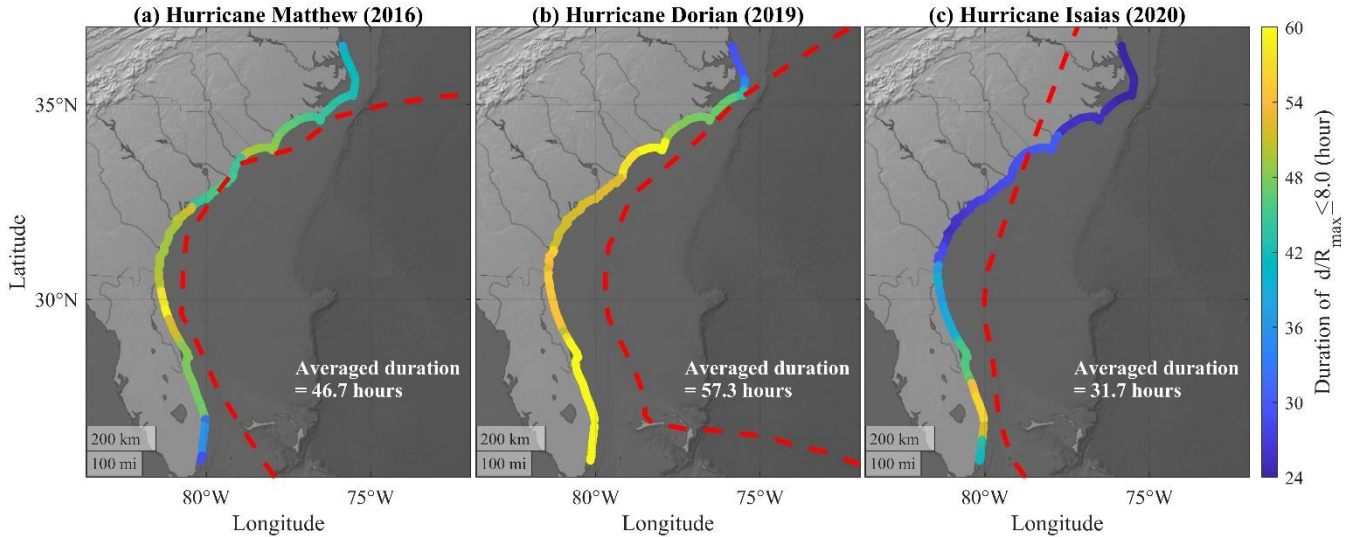
Figure 5. The durations of $d/R_{max} \leq 8.0$ along the SAB during three historical hurricanes. The red dashed curves represented the
315   **tracks obtained from IBTrACS database of each hurricane respectively.**

4.3 Relative contributions of η_S and R_2 to η_T

In addition to the peak η_T along the SAB during the three historical hurricanes, we compared the proportions of η_S, wave setup, and wave swash at three specified locations: Edisto Island, South Carolina (32.51°N, 80.26°W); Sea Island, Georgia (31.20°N, 81.33°W); and the barrier island south of Matanzas Inlet, Florida (29.68°N, 81.22°W) (Fig. 6). Edisto Island, South

320   Carolina (D_{crest}=2.10 m and D_{base}=1.26 m) and Sea Island, Georgia (D_{crest}=3.49 m and D_{base}=2.41 m) had relatively low dune elevations, in which dune overwash was more likely to occur during extreme weather events, according to the USGS (https://www.usgs.gov/news/national-news-release/fl-ga-sc-beaches-face-80-95-percent-chance-erosion-hurricane-matthew). The peak η_T south of Matanzas Inlet, Florida during the storms were 1.41 m to 1.62 m (51% to 64%) greater than the two other barrier islands mentioned above in the near–TC field during Matthew and Dorian (time instants shown by the vertical yellow

325   dash lines in Fig. 6). One of the factors causing higher estimated R_2 was the larger mean beach slope (β_m) at the barrier island south of Matanzas Inlet (0.151) compared to Sea Island (0.038) and Edisto Island (0.048) (Fig. A3 in the appendix). R_2 consisted of wave setup and wave swash. The percentage of wave swash in the peak η_T outnumbered that of wave setup by 25% to 34% at Sea Island and Edisto Island during all three TCs, while the wave swash only outnumbered wave setup by less than 9% at the barrier island south of Matanzas Inlet (Fig. A4 in the appendix). Meanwhile, we found that η_S contributed to

330   less than 40% in the peak η_T at the three locations as these three historical TCs approached. Surge levels at the peak η_T

generally decreased from south to north during the three hurricanes, whereas wave setup and wave swash did not experience such a pattern.
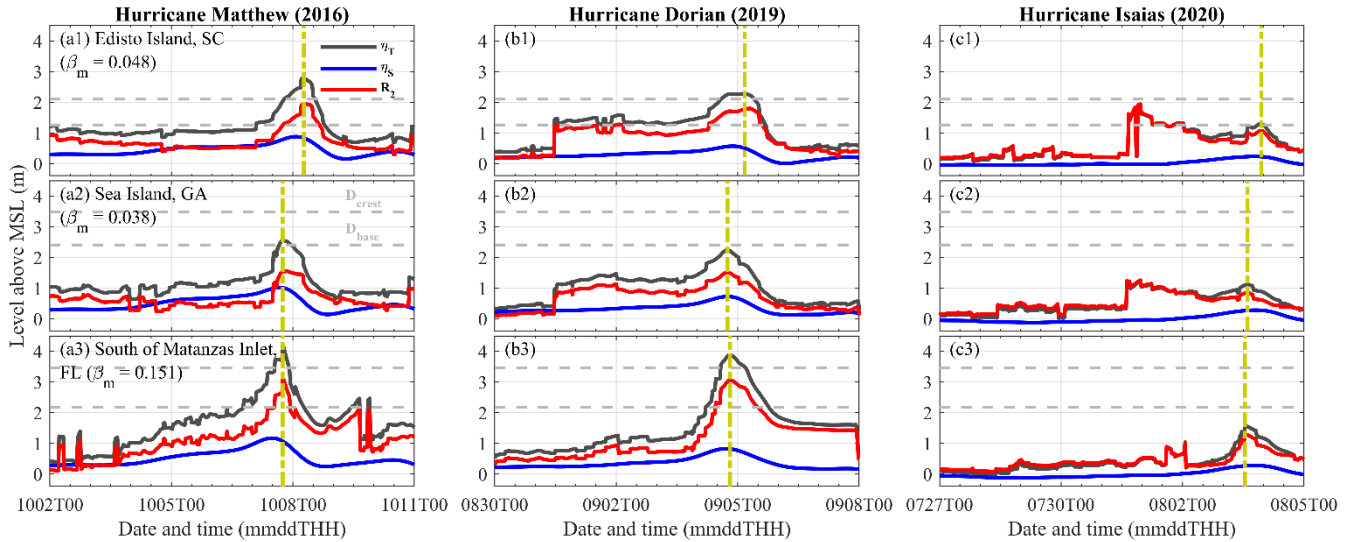
Figure 6. The time series of η_T (black curves), η_S (blue curves), and R_2 (red curves) at three selected locations during the three historical hurricanes. The horizontal gray dash lines were the local D_{crest} and D_{base} measured by USGS before Matthew (2016), and the vertical yellow dash lines were the peak η_T in the near–TC field.

Within the near–TC field, waves in most frequency bands kept receiving energy from the local wind, and η_T was directly impacted by the instantaneous TC characteristics. The peak η_T occurred within the near–TC field between 15:00 UTC 07 October 2016 and 07:00 UTC 08 October 2016 during Matthew, while it took place between 14:00 UTC 04 September 2019 and 04:00 UTC 05 September 2019 during Dorian (panels a1, a2, a3, b1, b2, and b3 in Fig. 6). The peak η_T at the three locations occurred in the near–TC field during Matthew and Dorian, without a second comparable peak η_T throughout the time series. The conditions during Isaias were unique and different from Matthew and Dorian. First, the instantaneous V_{max} did not reach 33 m s^{-1} during Isaias when $d/R_{max} \leq 8.0$ at most coastal sites along the SAB. Second, η_T generally experienced an abrupt increase before Isaias reached the coastal sites along the SAB. This earlier increase of η_T at Edisto Island (South Carolina) even exceeded the peak value within the near–TC field (panel c1 in Fig. 6). This increased η_T before the peak of the storm occurred between 21:00 and 23:00 UTC 31 July 2020 at Sea Island and Edisto Island, when Isaias was still far away from these three selected locations (i.e., with distances larger than 1300 km).

η_S and R_2 at the coast depended on the instantaneous TC characteristics within the near–TC field. The differences between the peak η_T within the near–TC field during hurricanes Matthew and Dorian were less than 1.0 m at the three selected locations. The peak η_T at the same locations during Hurricane Isaias within the near–TC field (03 August 2022 UTC) was 1.0 m to 2.7 m less than that of Matthew and Dorian. The η_S at the peak η_T during Isaias was 50% to 80% lower than that of Matthew and Dorian within the near–TC field at the three locations (numbers listed in Fig. A4 in the appendix). The R_2 (i.e., the sum of

setup and swash) at the peak η_T during Isaias was 40% to 60% smaller compared to that of Matthew and Dorian in the near–TC field. This was related to Isaias's smaller V_{max} within the SAB (28% to 36% smaller than Matthew and Dorian; Table 1).

355

Table 3. Maximum continuous durations of η_T and TWL over the local D_{base} at the three barrier islands during the three historical TCs in hours. T_{ETA} was the maximum continuous duration of the scenario $\eta_T \geq D_{base}$; T_{TWL} was the maximum continuous duration of the scenario $TWL \geq D_{base}$.

	T_{ETA} (hour)			T_{TWL} (hour)		
	Edisto Island	Sea Island	South of Matanzas Inlet	Edisto Island	Sea Island	South of Matanzas Inlet
Matthew	40.5	7.5	35.5	31.0	10.5	23.0
Dorian	125.0	0.0	37.0	24.5	6.0	24.0
Isaias	16.5	0.0	0.0	6.0	0.5	1.5

360 The duration of the same η_T category ($\eta_T \geq D_{crest}$; $D_{base} \leq \eta_T < D_{crest}$; and $\eta_T < D_{base}$) varied with TC characteristics. T_{ETA} at Edisto Island lasted up to more than five days during Dorian, which was much longer compared to the T_{ETA} during Matthew and Isaias (40.5 hours and 16.5 hours, respectively; Table 3). T_{ETA} at the barrier island south of Matanzas Inlet during Dorian (37.0 hours) was longer compared to Matthew (35.5 hours), but the difference was smaller than that at Edisto Island. While T_{ETA} primarily depends on TC characteristics, T_{TWL} also depends on the instantaneous local tidal range. The TWLs at tidal 365 troughs were lower with a larger tidal range. This led to a shorter T_{TWL} when compared to T_{ETA} in the three hurricanes, as TWLs dropped lower than D_{base} at tidal troughs. Although Dorian had a stronger V_{max} and slower V_t along the SAB on average, Matthew and Isaias had shorter distances to the coast. Moreover, the tidal range during Matthew was approximately 40 cm smaller compared to Dorian and Isaias on average at the eight NOAA tide gauges (shown in Fig. 1). With similar V_{max}, shorter distances to the coast and a smaller tidal range, Matthew had longer T_{TWL} at Edisto Island and Sea Island compared to 370 Dorian (Table 3).

4.4 Storm forced water level variation

Suh and Lee (2018) utilized two historical TCs to analyze and compare the propagation processes of forerunner surges and primary surges in the Yellow Sea, and these processes were linked to the heading direction, path, and translation speed of the storm. Similarly, we observed distinct patterns of storm–dependent water–level component variations during three different 375 storm events and at various locations along the SAB.

During Matthew and Dorian, the peak η_T occurred when the coastal sites started to be covered by the near–TC field, which was induced by the wind waves and η_S associated with higher TC intensities (i.e., larger pressure deficits and higher wind speeds). However, the η_T at the three coastal sites had another local maximum at 15:30 UTC 31 July 2020 during Isaias, when

the storm was still located around 21.5°N and 73.5°W, i.e., south of the SAB (Fig. 7b and Fig. 7d). This was primarily the

380 result of two factors. First, before entering the SAB (i.e., south of 26.0°N and east of 79.0°W), the translation speeds of Matthew (maximum of 7.52 m s^{-1} and average of 4.17 m s^{-1}) and Dorian (maximum of 7.35 m s^{-1} and average of 5.35 m s^{-1}) were slower compared to Isaias (maximum of 9.81 m s^{-1} and average of 6.74 m s^{-1}). Xu et al. (2007) found that the swell energy and wavelength increased when V_t was comparable to the group wave celerity and under 13 m s^{-1}. This allowed wind waves to experience an extended wind fetch and resulted in the growth of wavelength and wave height. According to Eq. 1 (Stockdon

385 et al., 2006), R_2 increases with the deep–water peak wavelength and the deep–water zero–order moment wave height. Second, before arriving at the Island of Hispaniola (19.0°N), the swell generated by Matthew on its right–hand side was blocked by the Island of Hispaniola and was unable to propagate towards the SAB on its path. By contrast, the swell generated by Isaias on its front–right quadrant was not blocked by any island (see Fig. 1). Thus, the condition during Isaias was better for swell's wavelength to be lengthened and to propagate ahead of the storm.
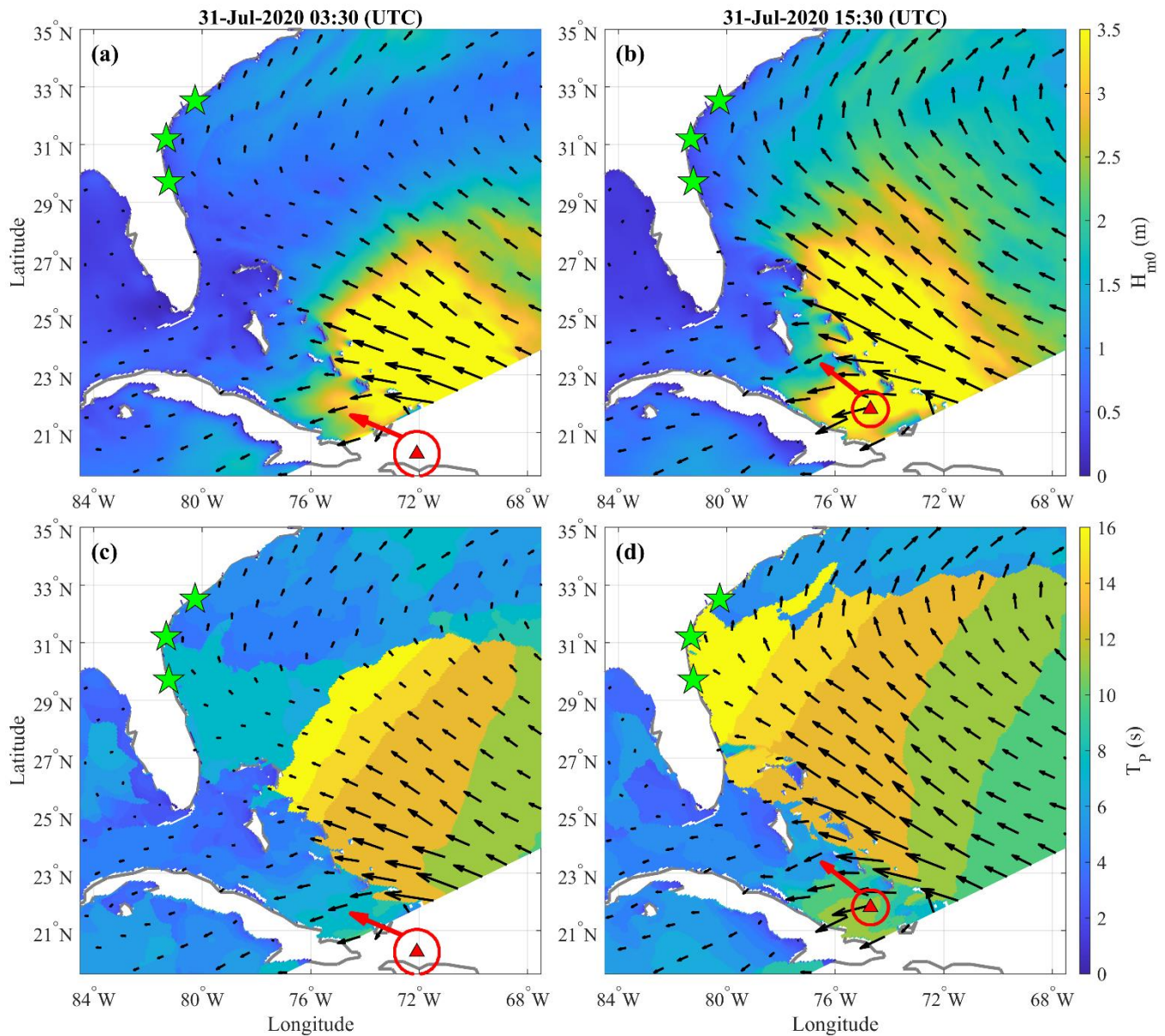
Figure 7. The propagation of the swells generated by Hurricane Isaias on its right-hand side. The green stars indicated the three selected barrier islands, i.e., Edisto Island, Sea Island, and the barrier island south of Matanzas Inlet (from North to South). The red triangles represented the eye of Isaias with the red circle denoting the instantaneous radius of maximum wind and the red arrow denoting the heading direction. The black arrows were the mean wave directions from COAWST simulation. The colormaps in panels (a) and (b) showed the distribution of H_{m0} at 03:30 UTC 31 July 2020 and 15:30 UTC 31 July 2020, respectively. The colormaps in panels (c) and (d) showed the distribution of T_P at 03:30 UTC 31 July 2020 and 15:30 UTC 31 July 2020, respectively.

According to the model results and linear wave dispersion relation, the peak wave period was 19.1 s and the corresponding deep–water phase celerity was larger than 25 m s^{-1} at Sea Island, Georgia at 15:30 UTC 31 July 2020 during Isaias (when the abrupt elevated R_2 occurred). This swell with a relatively long wave period generated by Isaias on its right–hand side arrived

400   at the SAB coast much earlier (one to two days) than the storm, which led to an abrupt increase in R_2. Around 16:00 UTC 01 August 2020, the instantaneous V_t of Isaias decreased from 7.0 m s^{-1} to less than 4.5 m s^{-1}. Additionally, waves with different periods travel with different phase celerities according to linear wave dispersion relation. This is also consistent with the distribution pattern of peak wave periods shown in Fig. 7c and Fig. 7d (i.e., waves with higher T_P moved forward faster and approached the SAB earlier). Consequently, the wavelength of the swell arriving later at the SAB decreased, which led to a

405   decrease of R_2.

4.5 Coastal impact regimes of Sallenger (2000) and the temporal variation of $\boldsymbol{\beta_m}$

The dune elevations measured by the USGS before Matthew did not reflect the realistic conditions during Dorian and Isaias, since the beach morphology (e.g., dune heights and beach slopes) changed in time. However, the time–invariant dune elevations allowed the present work to focus on determining the relative contributions of TC–induced water level components

410   (η_S and R_2) during various TCs. The coastal impact regimes (Sallenger, 2000) were determined with the relative *TWL*s depending on storm forced parameters (η_S and R_2), astronomic tides, and coastal morphology (dune elevations and beach slopes). However, the real coastal impact regimes during specific events require an update of the beach slopes and dune elevations. The problem was that this information was not always available at the spatial scale of this study.

To determine the sensitivity of the wave runup to the beach slopes, we used the post–Matthew β_m from Georgia to North

415   Carolina measured by USGS (Doran et al., 2017) to compare *TWL*s and T_{TWL} associated with the model results of Hurricane Dorian with the pre–Matthew surveyed β_m (Fig. 8). We used the post–Matthew beach morphological information to determine the difference in the estimated storm–induced water levels. The post–Matthew dataset showed that β_m experienced an averaged decrease of -0.026 after Hurricane Matthew. According to Eqs. 1 and 2, *TWL*s and T_{TWL} during Hurricane Dorian would decrease considering the change of β_m. Results showed that 50% of the coastal sites between Georgia and North

420   Carolina experienced an absolute difference of simulated peak *TWL* less than 0.5 m as β_m changed. The averaged decrease of peak *TWL* was 0.56 m with a standard deviation of 0.87 m. Meanwhile, an averaged decrease of T_{TWL} of 11.23 hours was observed (Fig. 8).

Based on Sallenger's (2000) categorizations, our model results showed that the at least 64.7% of the peak *TWL*s (i.e., the sum of η_T and astronomic tides; Table 2) belonged to the overwash and inundation regimes during the three hurricanes under the

425   assumption of constant dune elevations and β_m. However, dune heights and β_m are expected to decrease after storm events, which is consistent with the post–Matthew conditions from the observed data. While a decreased dune elevation led to more severe and longer impact regimes, a milder β_m resulted in a lower wave runup.
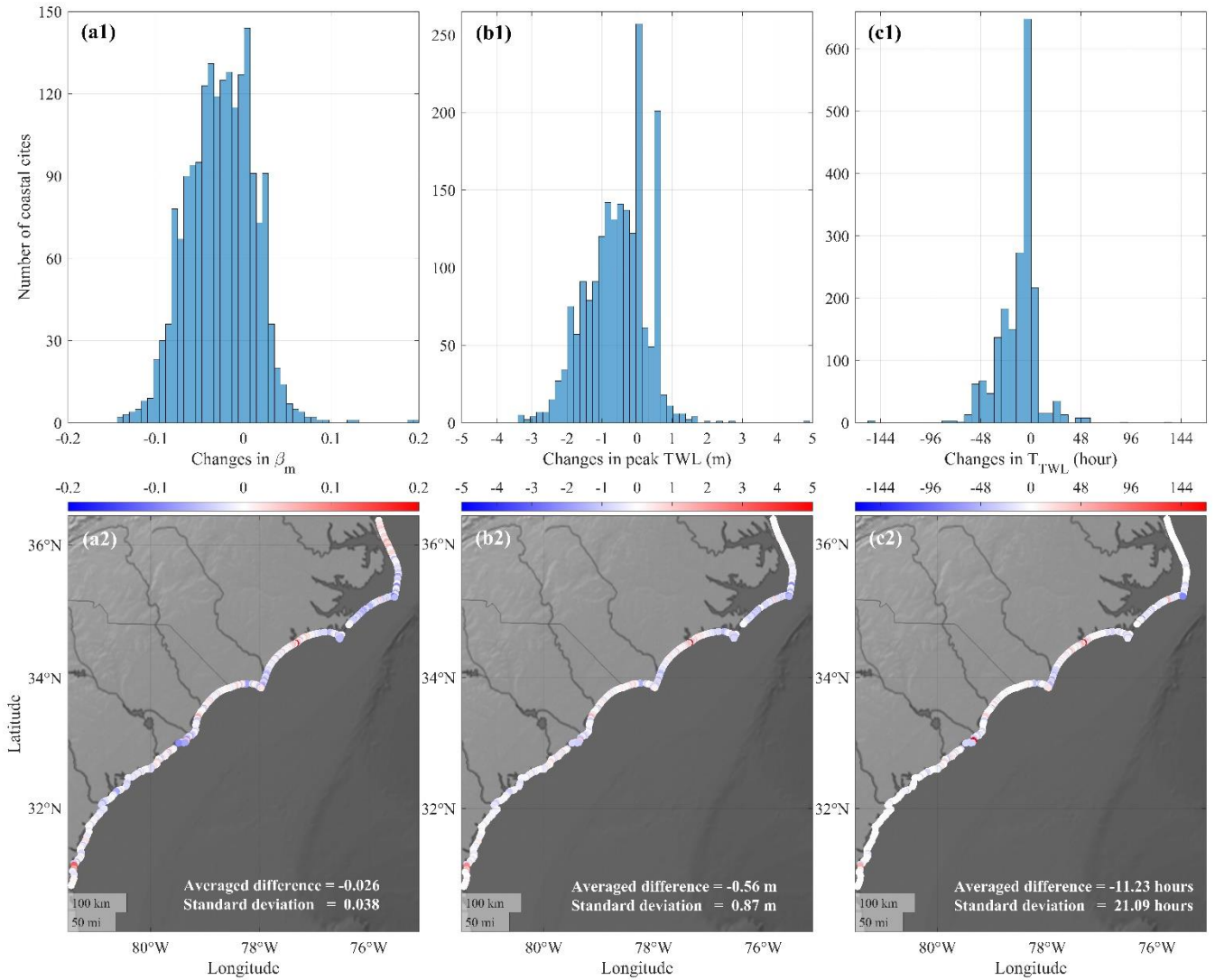
Figure 8. Histograms (top panels) and spatial distributions (bottom panels) of the differences of β_m, peak *TWL*, and T_{TWL} under pre– and post–Matthew conditions from Georgia to North Carolina coasts: a1, a2) β_m; b1, b2) peak *TWL*; c1, c2) T_{TWL}.

4.6 Arrival timing of the peak storm–dependent components

Beside beach morphology and TC–dependent parameters ($\eta_T = \eta_S + R_2$), TC–independent parameters like astronomic tides also influenced the coastal impact regimes. In some cases, the peak *TWL* exceeded D_{crest}, while the peak η_T did not exceed D_{crest}. This was related to the coincidence of the timing of the high tide and the peak η_T. In the case that the peak η_T occurred at low tide, the peak *TWL* would be lower than the peak η_T. With the time–invariant dune elevation, both the peak *TWL* and the peak η_T did not reach D_{crest} at this location during Dorian. However, both peak *TWL* and peak η_T would exceed D_{crest} in case that the dune elevation became lower.

4.7 Effects of TC properties on the durations of η_T

Hurricane Dorian traveled with a slow V_t (3.27 m s^{-1}) on average, which was not only slower than the other two historical storms but also slower than the global average of TCs in all categories (4.20 m s^{-1} to 6.00 m s^{-1}). While the instantaneous V_{max} had significant impacts on the η_T, the slow movement of the TC resulted in a longer duration of T_{ETA} at which a specific location was under its impact. The peak η_T did not reach D_{base} (T_{ETA}=0.0 hour) at Sea Island during Dorian while the peak η_T at the same location exceeded D_{base} for 6.0 hours during Matthew. V_t was the primary factor determining T_{ETA} at the other two coastal sites. However, as V_{max} increased and/or the distance to the TC eye decreased, T_{ETA} may also increase. The variations of T_{ETA} at the three coastal sites during the three historical TCs implied that the peak water level alone may not be sufficient to predict the coastal impacts in practical scenarios. For instance, T_{ETA} experienced a 67.7% difference (i.e., 84.5–hour difference) at Edisto Island between Matthew and Dorian (Table 3), while the peak η_T at this location belonged to the same categories during these two TCs.

4.8 Estimations of R_2 using different empirical formulas for R_2

Stockdon et al. (2006) used different formulas of R_2 for the scenarios $0.3 \leq \xi_0 < 4.0$ and $\xi_0 < 0.3$ (Eqs. 1 and 2). The range $0.3 \leq \xi_0 < 4.0$ represents intermediate to more reflective beach scenarios. The formula of Senechal et al. (2011) was proposed based on the regression of their observed runup data to improve the estimation under highly dissipative and saturated beach conditions ($\xi_0 < 0.3$) specifically (Eq. 4).

We compared the R_2 estimated by the formulas of Stockdon et al. (2006) and Senechal et al. (2011) at the same locations previously considered (Edisto Island, South Carolina; Sea Island, Georgia; and the barrier island south of Matanzas Inlet, Florida) during the three historical hurricanes (Fig. 9). The difference between the peak R_2 estimated by the two formulas reached up to 1.34 m at the barrier island south of Matanzas Inlet (panels a3 and b3 in Fig. 9; Stockdon's prediction was 76% higher than Senechal's prediction during Matthew and Dorian).
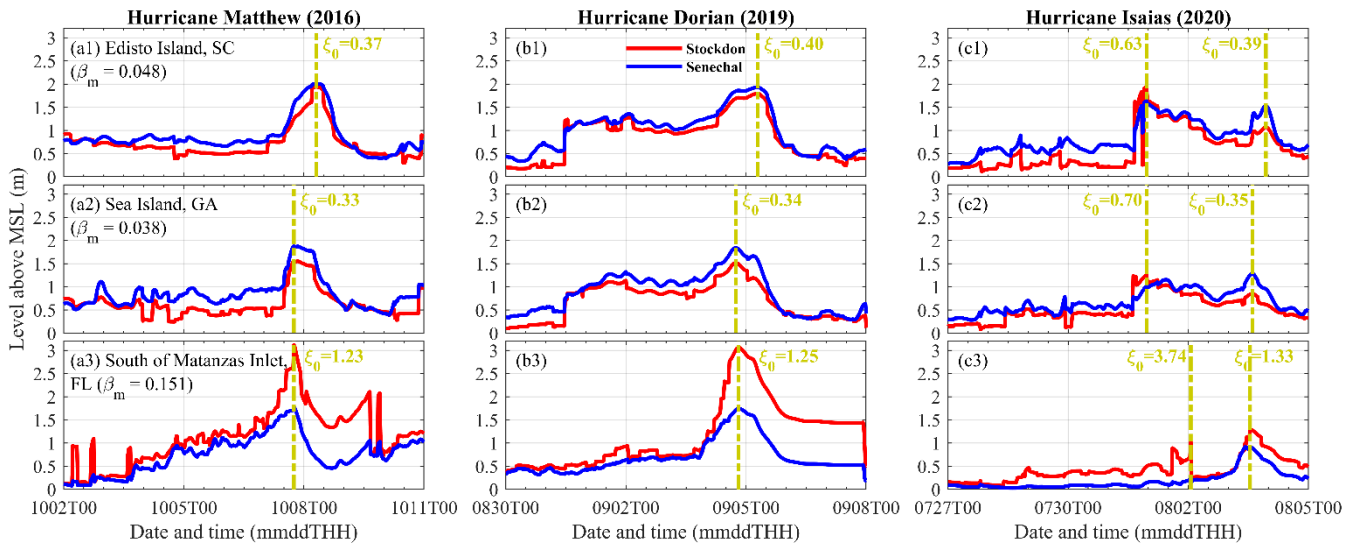
460 **Figure 9. The R_2 estimated by the formulas of Stockdon et al. (2006; red curves) and Senechal et al. (2011; blue curves) at three coastal sites during three hurricanes. The Iribarren numbers (ξ_0) corresponding to the peak R_2 (vertical yellow dash lines) were listed.**

The R_2 estimated by Stockdon's formula showed a distinctive pattern during Isaias: another peak occurred before the storm approached the observed location. This was related to Isaias's unique path and faster V_t. The R_2 by Senechal's formula did not

465 show this pattern, since Senechal et al. (2011) did not include the effect of L_0. The results showed that Stockdon's approach returned a larger R_2 compared to Senechal et al. (2011) especially under ξ_0>0.6 (with a difference up to 1.34 m). On the contrary, Senechal et al. (2011) gave larger values of R_2 under ξ_0<0.5 compared to the results by Stockdon et al. (2006) but with a smaller difference (i.e., less than 0.50 m).

We computed the differences between the time series of R_2 derived from the formulas of Stockdon et al. (2006) and Senechal

470 et al. (2011) (i.e., $\delta_R = R_{2-\text{Stockdon}} - R_{2-\text{Senechal}}$) along the SAB. Next, we calculated the correlation coefficients (C_{CORR}) between δ_R and five parameters: ξ_0, H_0, L_0, T_P, and β_m. It was found that β_m, ξ_0, and L_0 had higher C_{CORR}, which were 0.64, 0.47, and 0.42, respectively. δ_R increased as the mean beach slope, the Iribarren number, and the deep–water peak wavelength increased, which resulted in more reflective beach conditions. Stockdon's approach predicted that R_2 increased as wavelength increased under certain conditions (faster V_t and TC path allowing the swell to propagate toward the coasts).

475 **5 Conclusions**

We used the coupled ROMS–SWAN modeling system to simulate η_S and the wave fields (wave energy spectrum and bulk wave parameters) within the SAB during Matthew 2016, Dorian 2019, and Isaias 2020. Following Serafin and Ruggiero (2014), we used the measured η_0 and waves to estimate the *TWL*s from observations. We used the linear wave theory to calculate the deep–water wave parameters and estimate the 2% exceedance wave runup using Stockdon (2006)'s empirical

formula. We followed the same procedure with the results from COAWST and compared the *TWL*s estimated with both methods. COAWST model results showed good agreement with the peak *TWL*s, peak storm surges, peak wave runups, and exceedance durations.

We used our model results to compare the peak η_T along the SAB and at three coastal sites specifically. The instantaneous V_{max} and the distance to the hurricane eye were the key factors determining the peak η_T within the near–TC field, whereas the maximum continuous duration of η_T and *TWL*s over given thresholds were primarily determined by V_t and the distance to the hurricane eye. The contributions of wave runup (i.e., the sum of wave setup (16% to 38%) and wave swash (41% to 57%)) to the peak η_T was usually higher than η_S (17% to 40%) at the three selected coastal sites during the three historical TCs. The variability of η_S (up to 75%) at the peak η_T under different TC properties was larger than that of the wave runup (i.e., the sum of wave setup and wave swash; less than 59%). These wave–dependent parameters were not only functions of the TC characteristics but strongly depended on the local coastal morphology (e.g., beach slope). The time series of η_T revealed that with specific TC characteristics (e.g., path, heading direction, and V_t) the peak η_T may occur before the storm's peak (i.e., outside the near–TC field). This was observed in the case of Hurricane Isaias as the hurricane traveled with a fast instantaneous V_t (maximum of 9.81 m s^{-1} and average of 6.74 m s^{-1}, which was 1.1 to 2.3 times of the global average in all categories) two to three days before approaching the location.

Two empirical formulas of wave runup estimation were compared. Stockdon's formula predicted the extreme pre–storm swells associated with TC's faster translation speeds, whereas this peak was not observed when using Senechal's empirical formula. Since runup observations during these storms were unavailable, it was not possible to determine which empirical formula was giving the best predictions. Given the relevance of accurately estimating *TWL*s, more observations of the wave runup during TCs are needed for the verification and calibration of wave runup parameterizations. With the present analysis of historical storms, it was difficult to determine the individual effect of each TC characteristic on *TWL*s. Further numerical experiments and analysis employing synthetic and idealized TCs are needed to quantify the individual impacts of V_t, V_{max}, distance to the coast, and beach slope on *TWL*s and, thus, the coastal morphological impacts.

Data availability

The raw data of hurricane tracks is publicly available from the International Best Track Archive for Climate Stewardship (IBTrACS; https://www.ncei.noaa.gov/products/international-best-track-archive; accessed on 28 August 2023). The raw historical wave records used in the analysis are publicly available from the National Data Buoy Center Historical Data & Climatic Summaries (https://www.ndbc.noaa.gov/; accessed on 28 August 2023). The Rapid refresh re–analyzed atmospheric data used in this work is publicly available from the National Centers for Environmental Prediction (https://www.nco.ncep.noaa.gov/pmb/products/rap/; accessed on 18 August 2020). The Global Forecast System re–analyzed atmospheric data is publicly available from https://www.ncdc.noaa.gov/data-access/model-data/model-datasets/global-forecast-system-gfs (accessed on 18 August 2020). The Hybrid Coordinate Ocean Model (HYCOM) re–analyzed data used in

this work is publicly available from https://www.hycom.org/dataserver/gofs-3pt1/analysis (accessed on 31 March 2023). The information of tidal constituents is publicly available from Oregon State University TPXO Tide Model database (https://www.tpxo.net/home; accessed on 31 March 2023). The re–analyzed wave data used for the boundary conditions is publicly available from NOAA's WAVEWATCH III re–analyzed global dataset (https://polar.ncep.noaa.gov/waves/ensemble/download.shtml; accessed on 31 March 2023). Access to model results is available by contacting the authors.

CRediT authorship contribution statement

Chu-En Hsu: Conceptualization, Formal analysis, Investigation, Writing – original draft, Validation, Visualization. Katherine A. Serafin: Methodology, Supervision, Writing – review and editing. Xiao Yu: Supervision, Writing – review and editing. Christie A. Hegermiller: Methodology, Software, Writing – review and editing. John C. Warner: Methodology, Software, Writing – review and editing. Maitane Olabarrieta: Conceptualization, Funding acquisition, Methodology, Supervision, Writing – review and editing, Visualization.

Competing interests

The authors declare that they have no known competing financial interests or personal relationships that could have appeared to influence the work reported in this paper.

Acknowledgements

M. O. and C.-E. H. acknowledge the support from NSF thru the NSF Career-Award 1554892 and the USACE Engineering with Nature project (W912HZ-21-2-0035); M. O. and J. C. W. acknowledge support from the National Oceanographic Partnership Program (Project Grant N00014-21-1-2203). This support is gratefully acknowledged.

References

Alipour, A., Yarveysi, F., Moftakhari, H., Song, J. Y., Moradkhani, H.: A multivariate scaling system is essential to characterize the tropical cyclones' risk, Earth's Future, 10(5), https://doi.org/10.1029/2021EF002635, 2022.

Avila, L. A., Stewart, S. R., Berg, R., and Hagen, A. B.: Tropical cyclone report: Hurricane Dorian, National Hurricane Center Report. https://www.nhc.noaa.gov/data/tcr/AL052019_Dorian.pdf, 2020.

Battjes, J. A.: Surf similarity, Coastal Engineering Proceedings, 1(14), 26, https://doi.org/10.9753/icce.v14.26, 1974.

Benjamin, S. G., Weygandt, S. S., Brown, J. M., Hu, M., Alexander, C. R., Smirnova, T. G., Olson, J. B., James, E. P., Dowell, D. C., Grell, G. A., Lin, H., Peckham, S. E., Smith, T. L., Moninger, W. R., Kenyon, J. S., and Manikin, G. S.: A North

American hourly assimilation and model forecast cycle: The Rapid Refresh, Monthly Weather Review, 144(4), 1669–1694, https://doi.org/10.1175/MWR-D-15-0242.1, 2016.

Booij, N., Ris, R. C., and Holthuijsen, L. H.: A third-generation wave model for coastal regions – 1. Model description and validation, Journal of Geophysical Research: Oceans, 104(C4), 7649–7666, https://doi.org/10.1029/98jc02622, 1999.

Collins, C. O., Potter, H., Lund, B., Tamura, H., and Graber, H. C.: Directional wave spectra observed during intense tropical cyclones, Journal of Geophysical Research: Oceans, https://doi.org/10.1002/2017JC012943, 2018.

Doran, K. S., Long, J. W., Birchler, J. J., Brenner, O. T., Hardy, M. W., Morgan, K. L. M, Stockdon, H. F., and Torres, M. L.: Lidar-derived beach morphology (dune crest, dune toe, and shoreline) for U.S. sandy coastlines (ver. 4.0, October 2020): U.S. Geological Survey data release, https://doi.org/10.5066/F7GF0S0Z, 2017.

Doran, K. S., Long, J. W., and Overbeck, J. R.: A method for determining average beach slope and beach slope variability for U.S. Sandy Coastlines, U.S. Geological Survey Open-File Report 2015-1053, 5p., http://dx.doi.org/10.3133/ofr20151053, 2015.

Duchon, C. E.: Lanczos filtering in one and two dimensions, Journal of Applied Meteorology, 18(8), 1016–1022, https://doi.org/10.1175/1520-0450(1979)018%3C1016:LFIOAT%3E2.0.CO;2, 1979.

Egbert, G. D. and Erofeeva, S. Y.: Efficient inverse modelling of barotropic ocean tides, Journal of Atmosphere and Oceanic Technology, 19(2), 183–204, https://doi.org/10.1175/1520-0426(2002)019<0183:EIMOBO>2.0.CO;2, 2002.

Flather, R. A.: A tidal model of the northwest European continental shelf, Memoires de la Societe Royale de Sciences de Liege, 6, 141–164, 1976.

Hasselmann, K., Barnett, T. P., Bouws, E., Carlson, H., Cartwright, D. E., Enke, K., Ewingm J. A., Gienapp, H., Hasselmann, D. E., Kruseman, P., Meerburg, A., Muller, P., Olbers, D. J., Richter, K., Sell, W., and Walden, H.: Measurements of wind-wave growth and swell decay during the Joint North Sea Wave Project (JONSWAP), Deutschen Hydrographischen Zeitschrift. 12, A8, Hamburg, Germany, https://pure.mpg.de/pubman/faces/ViewItemOverviewPage.jsp?itemId=item_3262854, 1973.

Hasselmann, S., Hasselmann, K., Allender, J. H., and Barnett, T. P.: Computations and parameterizations of the nonlinear energy transfer in a gravity-wave spectrum. Part II: Parameterizations of the nonlinear energy transfer for application in wave models, Journal of Physical Oceanography, 15, 1378–1391, https://doi.org/10.1175/1520-0485(1985)015<1369:CAPOTN>2.0.CO;2, 1985.

Hegermiller, C. A., Warner, J. C., Olabarrieta, M., and Sherwood, C. R.: Wave-current interaction between Hurricane Matthew wave fields and the Gulf Stream, Journal of Physical Oceanography, 49(11), 2883–2900, https://doi.org/10.1175/jpo-d-19-0124.1, 2019.

Hsu, C.-E., Hegermiller, C. A., Warner, J. C., and Olabarrieta, M.: Ocean surface gravity wave evolution during three along–shelf propagating tropical cyclones: model's performance of wind-sea and swell, Journal of Marine Science and Engineering, 11(6), 1152, https://doi.org/10.3390/jmse11061152, 2023.

Irish, J. L. and Resio, D. T.: A hydrodynamics-based surge scale for hurricanes, Ocean Engineering, 37(1), 69–81, https://doi.org/10.1016/j.oceaneng.2009.07.012, 2010.

Irish, J. L., Resio, D. T., and Ratcliff, J. J.: The influence of storm size on hurricane surge, Journal of Physical Oceanography, https://doi.org/10.1175/2008JPO3727.1, 2008.

575 Kalourazi, M. Y., Siadatmousavi, S. M., Yeganeh-Bakhtiary, A., and Jose, F.: Simulating tropical storms in the Gulf of Mexico using analytical models, Oceanologia, https://doi.org/10.1016/j.oceano.2019.11.001, 2020.

Knapp, K. R., Diamond, H. J., Kossin, J. P., Kruk, M. C., and Schreck, C. J.: International Best Track Archive for Climate Stewardship (IBTrACS) Project, Version 4. NOAA National Centers for Environmental Information, https://doi.org/10.25921/82ty-9e16, 2018.

580 Komen, G. J., Hasselmann, S., and Hasselmann, K.: On the existence of a fully developed wind-sea spectrum, Journal of Physical Oceanography, 1271–1285, https://doi.org/10.1175/1520-0485(1984)014<1271:OTEOAF>2.0.CO;2, 1984.

Kumar, N., Voulgaris, G., Warner, J. C., and Olabarrieta, M.: Implementation of the vortex force formalism in the coupled ocean-atmosphere-wave-sediment transport (COAWST) modelling system for inner shelf and surf zone applications, Ocean Modelling, 47, 65–95, https://doi.org/10.1016/J.OCEMOD.2012.01.003, 2012.

585 Latto, A., Hagen, A., and Berg, R.: Tropical cyclone report: Hurricane Isaias. National Hurricane Center Report, https://www.nhc.noaa.gov/data/tcr/AL092020_Isaias.pdf, 2021.

Liu, H., Xie, L., Pietrafesa, L. J., and Bao, S.: Sensitivity of wind waves to hurricane wind characteristics, Ocean Modelling, 18(1), 37–52. https://doi.org/10.1016/J.OCEMOD.2007.03.004, 2007.

Madsen, O. S.: Spectral wave-current bottom boundary layer flows, Coastal Engineering Proceedings,
590 https://journals.tdl.org/icce/index.php/icce/article/view/4970, 1994.

Masson-Delmotte, V., Zhai, P., Pirani, A., Connors, S. L., Péan, C., Berger, S., Caud, N., Chen, Y., Goldfarb, L., Gomis, M. I., Huang, M., Leitzell, K., Lonnoy, E., Matthews, J. B. R., Maycock, T. K., Waterfield, T., Yelekçi, O., Yu, R., and Zhou, B.: Climate Change 2021: The Physical Science Basis, Contribution of Working Group I to the Sixth Assessment Report of the Intergovernmental Panel on Climate Change,
595 https://www.ipcc.ch/report/ar6/wg1/downloads/report/IPCC_AR6_WGI_TS.pdf, 2021.

Metzger, E. J., Smedstad, O. M., Thoppil, P. G., Hurlburt, H. E., Cummings, J. A., Wallcraft, A. J., Zamudio, L., Franklin, D. S., Posey, P. G., Phelps, M. W., Hogan, P. J., Bub, F. L., and DeHaan, C. J.: US Navy operational global ocean and Arctic ice prediction systems, Oceanography, 27(3), 32–43, http://dx.doi.org/10.5670/oceanog.2014.66., 2014.

Olabarrieta, M., Warner, J. C., and Hegermiller, C. A.: Development and application of an Infragravity Wave (InWave) driver
600 to simulate nearshore processes, Journal of Advances on Modeling Earth Systems, 15(6), https://doi.org/10.1029/2022MS003205, 2023.

Paniagua-Arroyave, J. F., Valle-Levinson, A., Parra, S. M., and Adams, P. N.: Tidal distortions related to extreme atmospheric forcing over the inner shelf, Journal of Geophysical Research: Oceans, 124(9), 6433–6734, https://doi.org/10.1029/2019JC015021, 2019.

605   Parker, K., Erikson, L., Thomas, J., Nederhoff, K., Barnard, P., and Muis, S.: Relative contributions of water-level components to extreme water levels along the U.S. Southeast Atlantic Coast from a regional-scale water-level hindcast, Natural Hazards, 117, 2219–2248, https://doi.org/10.1007/s11069-023-05939-6, 2023.

Roelvink, D., Reniers, A., van Dongeren, A., van Thiel de Vries, J., McCall, R., and Lescinski, J.: Modelling storm impacts on beaches, dunes, and barrier islands, Coastal Engineering, 56(11-12), 1133–1152,
610   https://doi.org/10.1016/j.coastaleng.2009.08.006, 2009.

Sallenger Jr., A. H.: Storm impact scale for barrier islands, Journal of Coastal Research, 16, 890–895, https://www.jstor.org/stable/4300099, 2000.

Senechal, N., Coco, G., Bryan, K. R., and Holman, R. A.: Wave runup during extreme storm conditions, Journal of Geophysical Research: Oceans, 116(7), https://doi.org/10.1029/2010JC006819, 2011.

615   Serafin, K. A. and Ruggiero, P.: Simulating extreme total water levels using a time-dependent, extreme value approach, Journal of Geophysical Research: Oceans, 119(9), 6305–6329, https://doi.org/10.1002/2014JC010093, 2014.

Shchepetkin, A. F. and McWilliams, J. C.: The regional oceanic modelling system (ROMS): A split-explicit, free-surface, topography-following-coordinate oceanic model, Ocean Modelling, https://doi.org/10.1016/j.ocemod.2004.08.002, 2005.

Shi, F., Kirby, J. T., Harris, J. C., Geiman, J. D., Grilli, S. T.: A high-order adaptive time-stepping TVD solver for Boussinesq
620   modeling of breaking waves and coastal inundation, Ocean Modelling, 43–44, 36–51, https://doi.org/10.1016/j.ocemod.2011.12.004, 2012.

Stewart, S. R.: Tropical cyclone report: Hurricane Matthew. National Hurricane Center Report, https://www.nhc.noaa.gov/data/tcr/AL142016_Matthew.pdf, 2017.

Stockdon, H. F., Holman, R. A., Howd, P. A., and Sallenger Jr., A. H.: Empirical parameterization of setup, swash, and runup,
625   Coastal Engineering, 53(7), 573–588, https://doi.org/10.1016/j.coastaleng.2005.12.005, 2006.

Stockdon, H. F., Sallenger Jr., A. H., Holman, R. A., and Howd, P. A.: A simple model for the spatially-variable coastal response to hurricanes, Marine Geology, 238(1-4), 1–20, https://doi.org/10.1016/j.margeo.2006.11.004, 2007.

Stockdon, H. F., Thompson, D. M., Plant, N. G., Long, J. W.: Evaluation of wave runup predictions from numerical and parametric models, Coastal Engineering, 92, 1–11, https://doi.org/10.1016/j.coastaleng.2014.06.004, 2014.

630   Suh, S. W. and Lee, H. Y.: Forerunner storm surge under macro-tidal environmental conditions in shallow coastal zones of the Yellow Sea, Continental Shelf Research, 169, 1–16, https://doi.org/10.1016/j.csr.2018.09.007, 2018.

Taylor, P. K. and Yelland, M. J.: The Dependence of sea surface roughness on the height and steepness of the waves, Journal of Physical Oceanography, 31(2), 572–590, https://doi.org/10.1175/1520-0485(2001)031<0572:TDOSSR>2.0.CO;2, 2001.

The WAVEWATCH III Development Group: User manual and system documentation of WAVEWATCH III version 5.16.
635   NOAA / NWS / NCEP / MMAB Technical Note 329, https://polar.ncep.noaa.gov/waves/wavewatch/manual.v5.16.pdf, 2016.

Uchiyama, Y., McWilliams, J. C., and Shchepetkin, A. F.: Wave–current interaction in an oceanic circulation model with a vortex-force formalism: Application to the surf zone, Ocean Modelling, 34(1–2), 16–35, https://doi.org/10.1016/j.ocemod.2010.04.002, 2010.

Wang, K., Hou, Y., Li, S., Du, M., Chen, J., and Lu, J.: A comparative study of storm surge and wave setup in the East China

640   Sea between two severe weather events, Estuarine, Coastal and Shelf Science, https://doi.org/10.1016/j.ecss.2020.106583, 2020.

Warner, J. C., Sherwood, C. R., Signell, R. P., Harris, C. K., and Arango, H. G.: Development of a three-dimensional, regional, coupled wave, current, and sediment-transport model, Computers and Geosciences, 34(10), 1284–1306, https://doi.org/10.1016/j.cageo.2008.02.012, 2008.

645   Warner, J. C., Armstrong, B., He, R., and Zambon, J. B.: Development of a Coupled Ocean-Atmosphere-Wave-Sediment Transport (COAWST) Modelling System, Ocean Modelling, https://doi.org/10.1016/j.ocemod.2010.07.010, 2010.

Xu, F., Perrie, W., Toulany, B., and Smith, P. C.: Wind-generated waves in Hurricane Juan, Ocean Modelling, 16(3–4), 188–205, https://doi.org/10.1016/J.OCEMOD.2006.09.001, 2007.

Young, I. R.: Directional spectra of hurricane wind waves, Journal of Geophysical Research: Oceans,

650   https://doi.org/10.1029/2006JC003540, 2006.

Appendices
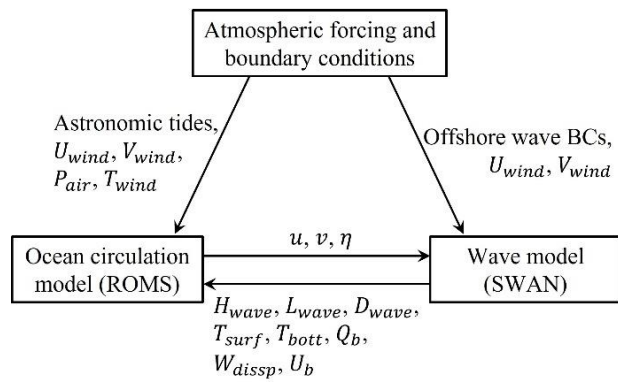
Figure A1. Computational flowchart of ocean circulation-wave coupling using COAWST modeling system.
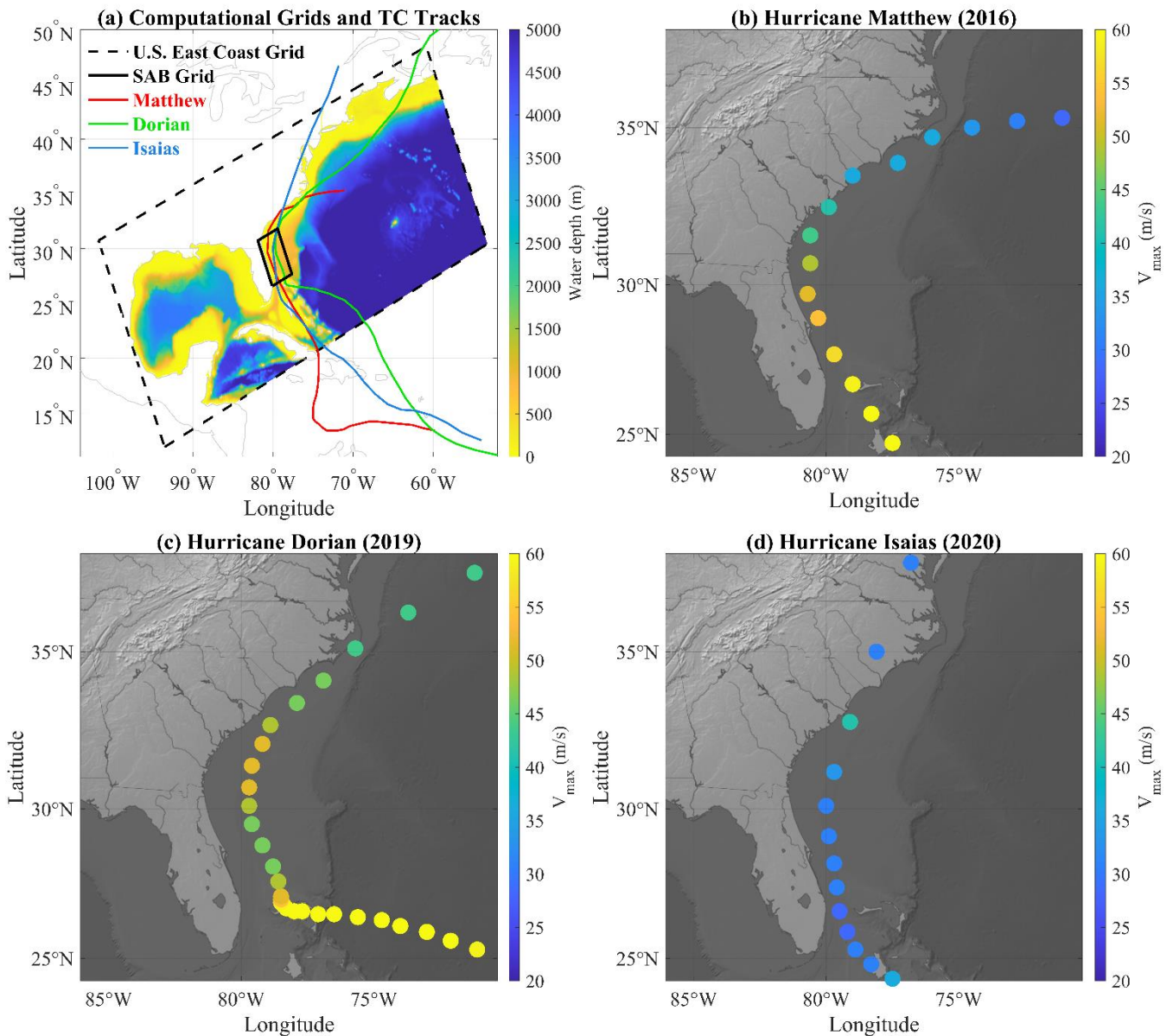
655

Figure A2. a) IBTrACS (International Best Track Archive for Climate Stewardship) data of the three TCs and computational domain and bathymetry (red: Matthew; green: Dorian; blue: Isaias; black: the boundaries of computational grids; hypsometric map: water depth). Panels b), c), and d) illustrated the tracks of the TCs (dots position), with the colormap of circles representing the maximum sustained wind during Hurricanes Matthew, Dorian, and Isaias, respectively. The time interval between adjacent dots
660   was 6 hours.
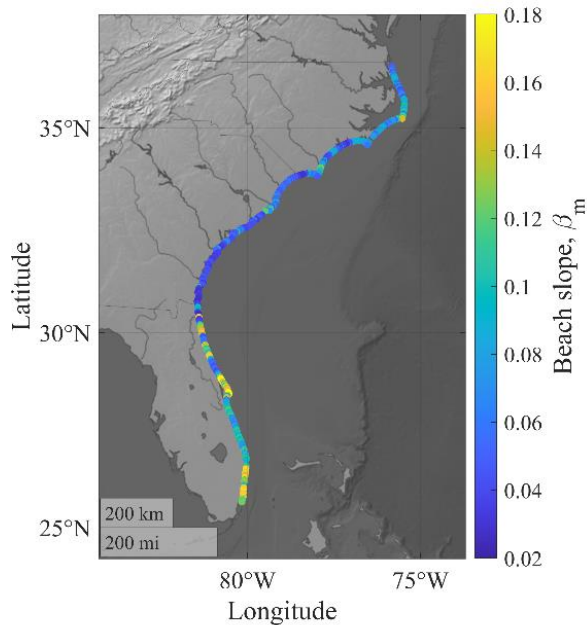
Figure A3. Pre-Matthew mean beach slopes along the SAB measured by USGS.

665
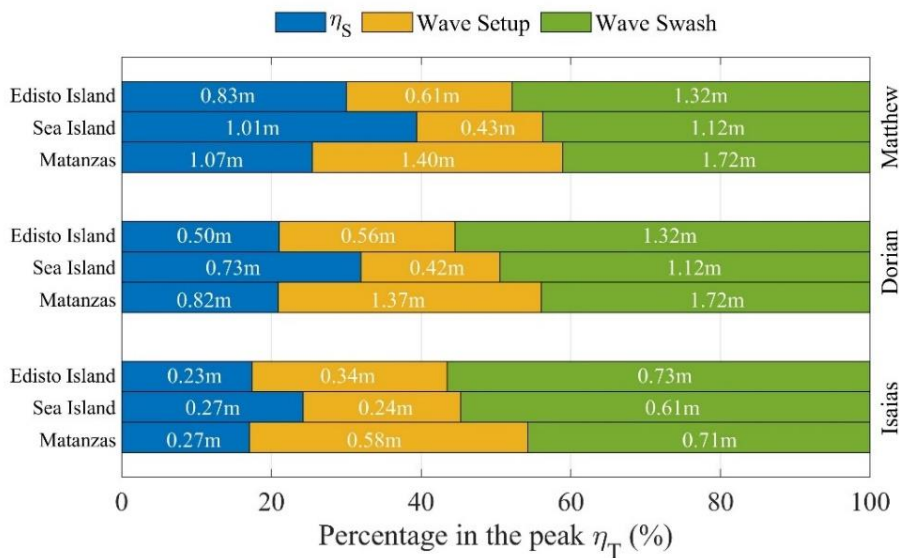
Figure A4. The contributions of η_S, wave setup, and wave swash in the peak η_T during the three historical hurricanes at the three coastal sites: South of Matanzas Inlet, Florida; Sea Island, Georgia; and Edisto Island, South Carolina with the corresponding contribution of each component (%) in the peak η_T and the level listed by the number written in white font.